

Second Harmonic Generation and Confined Acoustic Phonons in Highly Excited Semiconductor Nanocrystals[†]

Dong Hee Son,[‡] Joshua S. Wittenberg, Uri Banin,[§] and A. Paul Alivisatos*

Department of Chemistry, University of California, Berkeley, California 94720, Materials Sciences Division, Lawrence Berkeley National Laboratory, Berkeley, California 94720, and Department of Chemistry, The Hebrew University of Jerusalem, Jerusalem, Israel 91904

Received: April 1, 2006; In Final Form: August 11, 2006

The photo-induced enhancement of second harmonic generation and the effect of nanocrystal shape and pump intensity on confined acoustic phonons in semiconductor nanocrystals have been investigated with time-resolved scattering and absorption measurements. The second harmonic signal showed a sublinear increase of the second-order susceptibility with respect to the pump pulse energy, indicating a reduction of the effective one-electron second-order nonlinearity with increasing electron–hole density in the nanocrystals. The coherent acoustic phonons in spherical and rod-shaped semiconductor nanocrystals were detected in a time-resolved absorption measurement. Both nanocrystal morphologies exhibited oscillatory modulation of the absorption cross section, the frequency of which corresponded to their coherent radial breathing modes. The amplitude of the oscillation also increased with the level of photoexcitation, suggesting an increase in the amplitude of the lattice displacement as well.

1. Introduction

The dependence of the electronic structure and charge carrier interaction of semiconductor nanocrystals on the size and shape are perhaps their most prominent material properties.^{1–3} Continuous tuning of the band-edge absorption and emission wavelengths and control of the pathways and rates of charge carrier relaxation can be realized by varying the size, shape, and interfacial structure of the nanocrystals. So far, the majority of studies of the size- and shape-dependent optical and electronic properties have been performed under conditions where the density of photogenerated charge carriers is small.^{1,3–5} The average number of electron–hole pairs created by photoexcitation was typically from less than one to a few per particle. On the other hand, the properties of semiconductor nanocrystals with a large number of electron–hole pairs, e.g., tens to hundreds per nanocrystal, have received much less attention.⁶

In bulk semiconductors, the effects of creating dense electron–hole pairs on their optical and electronic properties have been relatively well studied. Band gap renormalization and the onset of metallic reflectivity have been observed in bulk semiconductors with a high density of charge carriers, e.g., $>10^{21}/\text{cm}^3$.^{7–9} When the electron–hole density reaches about 10% of the atom density or higher, its influence on the electronic structure becomes drastic. From direct coupling of the electron–hole plasma and the lattice, nonthermal melting occurs before the electronic energy is transferred to the crystal lattice.^{10,11}

In principle, all the processes responsible for the bulk phenomena are operating also in nanocrystals under the influence of spatial confinement. The effect of size reduction on nanocrystals in the high electron–hole density regime is, however, more complex than in the low electron–hole density

regime. In addition to the usual quantum confinement effect on the charge carriers, suppression of carrier diffusion, thermal gradients, and mechanical stress, which affect the optical and structural properties in bulk semiconductors, has to be considered. Moreover, the dense electron–hole pairs in semiconductor nanocrystals should behave more like an electron–hole plasma with very weak interactions as compared to those of bound electron–hole pairs. When the electron–hole density is sufficiently high, they may even look like metallic nanocrystals. In this case, the influence of spatial confinement on the electronic properties of semiconductor nanocrystals of high electron–hole density can be significantly different from those of low electron–hole density. At even higher excitation intensities, melting (either nonthermal or thermal) may occur. There are pronounced size effects on the phase diagram of nanocrystals, and the thermal melting point is generally inversely related to size, decreasing in hundreds of degrees for particles with diameters of few nanometers.¹² This is due to the dramatic increase in the contribution of the surface energy term to the free energy in the small particles.

In this work, we created a high density of electron–hole pairs in colloidal semiconductor nanocrystals and studied their effect on the optical nonlinearity and structural properties of the nanocrystals. The highest excitation intensity in this study brings us closer to accessing the melting regime in nanocrystals.¹³ Our interest was in the photoinduced enhancement of the second harmonic generation (SHG) and on acoustic phonons in colloidal semiconductor nanocrystals. In particular, SHG is sensitive to both the electronic excitation and structural order, and was previously used to probe melting processes in bulk semiconductors. Here, time-resolved measurements of the enhancement of SHG signals at various photoexcitation intensities were made to investigate the second-order optical nonlinearity in CdTe nanocrystals with dense electron–hole pairs under spatial confinement. Generation of dense electron–hole pairs by a short and intense laser pulse in semiconductor nanocrystals can also

[†] Part of the special issue “Charles B. Harris Festschrift”.

* Corresponding author. E-mail: alivis@berkeley.edu.

[‡] Current address: Department of Chemistry, Texas A&M University, College Station, Texas 77842.

[§] Department of Chemistry, The Hebrew University of Jerusalem.

create coherent lattice motions. They are capable of directly affecting the optical and electronic properties via structural modification.^{14,15} In addition, coherent lattice displacements can play a crucial role in phase transitions if the displacement of atoms can assist the nanocrystals in reaching the transition state.¹⁶ Here we studied the shape and excitation intensity dependence of the frequency and the amplitude of the coherent acoustic phonon modes in CdSe nanocrystals, also as a step toward time-resolved study of melting in nanocrystals. From a simple analysis of the optical signature of the coherent acoustic modes, we infer the relationship between the response of the lattice and the level of excitation of the charge carriers in semiconductor nanocrystals.

2. Experimental Section

In this study, chemically synthesized colloidal nanocrystals of CdSe and CdTe were used. Spherical and rod-shaped CdSe and CdTe nanocrystals were synthesized following published procedures.^{1,2} These nanocrystals were dispersed stably in cyclohexane, which was used as the solvent.

The laser system used was a regeneratively amplified Ti:sapphire laser (Spitfire, Spectra Physics), which produces 1 mJ pulses of 40 fs (fwhm), centered at 800 nm at a repetition rate of 1 kHz. The output beam was split into two or three beams depending on the specific setup required for each experiment. One beam was frequency-doubled in a type-I, β -barium borate (BBO) crystal to generate 400 nm pump beams. Before the BBO crystal, a half-wave plate and a polarizer were placed to continuously vary the intensity of the 400 nm beam for the pump-intensity-dependent study. The second 800 nm beam was focused on a 1 mm thick sapphire crystal to generate a white light continuum. This served either as the probe beam in the absorption measurement or as the seed beam for the home-built optical parametric amplifier (OPA). The spectral bandwidth of the continuum light was controlled by adjusting the width of the slit in a prism chirp compensator. The OPA had a single-pass noncollinear configuration using a type-II BBO crystal as the nonlinear medium. The BBO crystal was pumped by 400 nm beam, which was produced by frequency-doubling the third 800 nm beam in another type-I BBO crystal. The near-infrared portion of the white light continuum was used as the seed for the OPA. Signal and idler beams were generated in the near-infrared and visible ranges, respectively. The signal beam at 880 nm was used for the study of excitation-induced second harmonic generation to avoid the strong background scattering from the 400 nm excitation pulses. Typically, an 880 nm signal beam with 1–2 μ J pulse energy was generated from the 400 nm OPA pump beam with >30 μ J pulse energy. Beam sizes (fwhm) of the pump and probe beams were 150 μ m and >50 μ m, respectively, in all the experiments.

For the measurement of the time-resolved second harmonic signal from the photoexcited nanocrystals, 400 nm pump and 880 nm probe light were used. Incoherent hyper-Rayleigh scattering occurring at 440 nm was collected at less than 90 degrees with respect to the pump beam direction. The time resolution of the measurement was \sim 100 fs. The second harmonic signal was either detected by a charge-coupled device (CCD) in conjunction with a spectrograph or a photomultiplier tube (PMT). The signal from the PMT was fed into a lock-in amplifier synchronized to the chopping frequency (500 Hz) of the probe beam. For the transient absorption measurement, two photodiodes (PD) were used for the reference and the sample probe beams. The signals from the PDs were further averaged and processed with boxcar-gated integrators and an analogue processor.

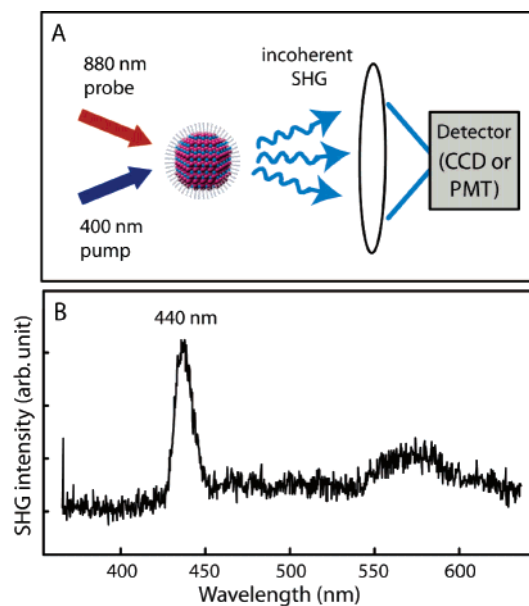


Figure 1. (A) Schematic description of the experimental setup for the measurement of the time-resolved second harmonic generation from CdTe nanocrystals. (B) Second harmonic signal from spherical CdTe nanocrystals obtained with 880 nm probe without photoexcitation.

In all the experiments, the nanocrystal solutions were continuously circulated through a jet nozzle to produce a free streaming jet in order to prevent complications due to repeated irradiation of the same sample area with intense UV light. The thickness of the sample solution jet was 200 μ m. The absorption spectra of the sample solution taken before and after the experiment showed no difference, indicating the absence of noticeable degradation of the sample solutions during the experiments.

3. Results

We used two complementary phenomena, SHG and coherent acoustic phonons, to study the effect of excitation of large numbers of electron–hole pairs in semiconductor nanocrystals. In either case, we do not yet reach the melting regime, but we are approaching it and can see various effects of the intense excitation on the signals as discussed below.

3.1. Photoinduced Enhancement of the Second Harmonic Generation in CdTe Nanocrystals. Figure 1A shows a simple schematic description of the measurement of the second harmonic generation (SHG) from photoexcited nanocrystals. The apparatus was set up in the pump–probe configuration, where variably time-delayed 880 nm light probed the time-dependent SHG signal from the photoexcited nanocrystals. In Figure 1B, a typical SHG spectrum from 7 nm CdTe nanocrystals recorded with 880 nm probe light only is shown. The SHG signal at 440 nm observed in CdTe nanocrystals is from incoherent hyper-Rayleigh scattering (HRS) of the incident beam.¹⁷ The intensity of SHG signal, $I(2\omega)$, arising from hyper-Rayleigh scattering of the incident beam of intensity $I(\omega)$ by colloidal solution of nanocrystals can be written as follows.¹⁸

$$I_{\text{SHG}}(2\omega) = G(N_s \langle \beta_s^2 \rangle + N_{\text{nc}} \langle \beta_{\text{nc}}^2 \rangle) I(\omega)^2$$

N_s and N_{nc} are the number concentrations of solvent and nanocrystal, respectively. $\langle \beta_s^2 \rangle$ and $\langle \beta_{\text{nc}}^2 \rangle$ represent the square of the first hyperpolarizability of solvent molecule and nanocrystal, respectively, averaged over the distribution of angular orientation of the molecules in the isotropic solution. G is a

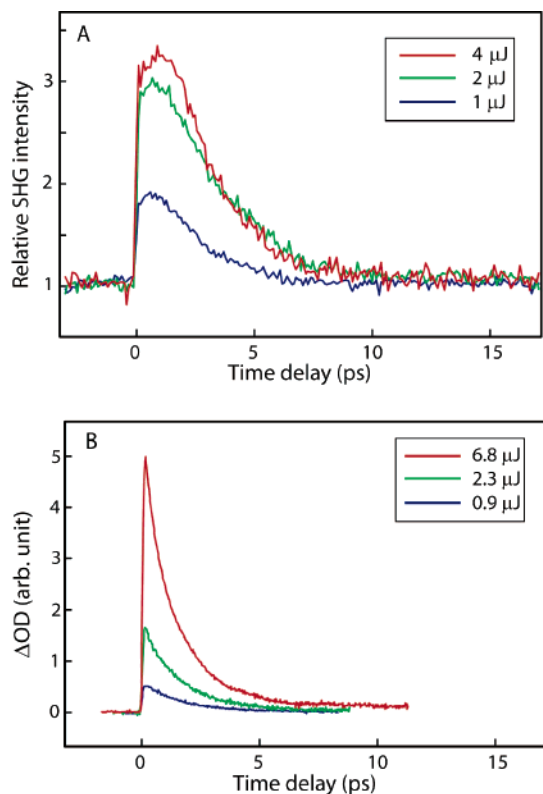


Figure 2. (A) Time-resolved second harmonic generation and (B) time-resolved absorption from CdTe nanocrystals obtained with 400 nm pump and 880 nm probe. The second harmonic signals are normalized to the signal at negative time delay to show the relative enhancement.

constant that depends on the geometry of measurement and local field factors. At a typical nanocrystal concentration of $\sim 10^{15}/\text{cm}^3$, solvent molecules (cyclohexane) had a negligible contribution to the overall SHG signal. At wavelengths near 600 nm and longer, a two-photon fluorescence signal from the CdTe nanocrystals was noticeable when the pulse energy of the 880 nm probe light was higher than $\sim 2 \mu\text{J}$. In this study, we set the probe pulse energy below $1 \mu\text{J}$ to minimize the interference from two-photon fluorescence. When the PMT was used in the time-resolved measurement, a narrow band-pass filter (440 nm, fwhm = 10 nm) was placed in front of the PMT to minimize the scattered pump and fluorescence light reaching the detector.

Time-dependent SHG signals from 7 nm spherical CdTe nanocrystals after photoexcitation are shown in Figure 2A at several different pump pulse energies. The SHG signals are normalized to the signal at negative pump–probe time delay to show the relative enhancement of the SHG signal. Blocking the pump light from the sample gave the same level of SHG signal at negative time delays as with both pump and probe lights present. The nonenhanced SHG signals at negative time delays were independent of the pump pulse energy up to $\sim 4 \mu\text{J}$, although the overall signal became noisier with increasing pump pulse energy. At higher pump pulse energies, the signal from the lock-in amplifier decreased due to the strong background from the tail of the pump-induced fluorescence and the limited linearity of the PMT. This limited our ability to probe the transient SHG response above the $\sim 4 \mu\text{J}$ pump intensity.

At all of the pump pulse energies shown in Figure 2A, the SHG signal shows instrument response limited rises upon the photoexcitation of the electron–hole pairs. The SHG signal subsequently decays back to the initial intensity within a few picoseconds, although it does not follow simple exponential decay kinetics. Similar increases in the SHG signal after

photoexcitation have been observed earlier on the surfaces of bulk gold, and silicon with a native oxide overlayer, in surface SHG measurements.^{19,20} On the other hand, decreases in SHG signal after photoexcitation have also been observed in *p*-nitroaniline and a single ZnO nanowire.^{21,22} The photoinduced enhancement of SHG on gold surface has been explained in terms of the increased overlap of the states involved in two-photon excitation and de-excitation due to the broadened Fermi–Dirac distribution of the electrons. On silicon surfaces, the mechanism for the SHG enhancement is less clear because the surface composition (oxide terminated vs H terminated) has a large effect on the SHG. In the case of *p*-nitroaniline and ZnO nanowire, diminution of the SHG was explained in terms of reduced anisotropy of the excited-state charge distribution resulting in a decrease of the effective second-order nonlinear susceptibility. The increase of the SHG after photoexcitation in CdTe nanocrystals indicates that the conduction band electrons exhibit a stronger second-order nonlinear response than the valence band electrons.

The time-dependence of the SHG signal in photoexcited bulk semiconductors and metals has often been ascribed to the relaxation of the photoexcited carriers.^{22,23} The 1/e decay time of the SHG signals shown Figure 2A is ~ 3 ps, which becomes only slightly longer with increasing pump pulse energy. In further analysis of the data, we used the relative enhancement of the apparent macroscopic second-order electric susceptibility, $\chi_{\text{rel}}^{(2)}(t)$, instead of the time-dependent SHG signal, $I_{\text{SHG}}(t)$. $\chi_{\text{rel}}^{(2)}(t)$ was calculated simply by taking the square root of the relative SHG signal enhancement after photoexcitation.

$$\chi_{\text{rel}}^{(2)}(t) = \sqrt{\langle \beta_{\text{nc}}^2(t) \rangle / \langle \beta_{\text{nc}}^2(t < 0) \rangle} = \sqrt{I_{\text{SHG}}(t) / I_{\text{SHG}}(t < 0)}$$

For this calculation, a small correction was made to the raw SHG signal in order to compensate for the absorption of probe light and SHG signal by the sample. This was accomplished by measuring the time-dependent absorption at 880 and 440 nm independently on the same sample and correcting for the attenuation of the light at each wavelength. This correction was only a few percent of the raw SHG signal. The resulting $\chi_{\text{rel}}^{(2)}(t)$ -traces also have decay time scales of ~ 3 ps.

In semiconductor nanocrystals such as CdSe and CdTe, carrier relaxation can also be probed by monitoring the pump-induced carrier absorption in the near-infrared spectral region, where intraband absorption occurs.⁵ The time scale of pump-induced absorption decay measured at 880 nm probe wavelength was ~ 2 ps, which is shorter than the SHG signal decay time (Figure 2B). Considering that the induced absorption decay time is dependent on the probe wavelength, the discrepancy in the two decay time scales is considered not significant. The consistency of the observed decay time of the transient SHG signal with that of the typical carrier relaxation time scale leads us to assign the observed decay in the SHG enhancement to this carrier relaxation process. This strongly supports our picture of SHG enhancement due to the highly excited conduction band electrons.

On the other hand, there is a more distinct difference in the dependence of signal intensity on the pump pulse energy between $\chi_{\text{rel}}^{(2)}(t)$ and the pump-induced absorption. In the case of the pump-induced absorption, the peak absorption intensity, near zero time delay, increased linearly with respect to the pump pulse energy. On the other hand, the peak value of $\chi_{\text{rel}}^{(2)}(t)$, denoted $\chi_{\text{rel,peak}}^{(2)}$ hereafter, increased sublinearly as the pump pulse energy became higher. The linear increase of the pump-induced carrier absorption indicates that the photoexcitation of

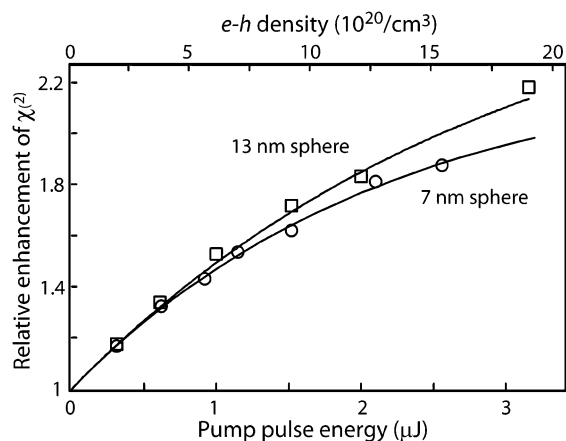


Figure 3. Pump pulse energy dependence of $\chi_{\text{rel,peak}}^{(2)}$ (peak value of $\chi_{\text{rel}}^{(2)}(t)$) for the spherical CdTe nanocrystals. The top axis indicates the average electron–hole density in the nanocrystals calculated within the probe area at the corresponding pump pulse energy. See the text for the definition of $\chi_{\text{rel}}^{(2)}(t)$.

carriers is in the linear regime, where the initially excited carrier density is proportional to the laser pulse energy. Being in the linear excitation regime was also corroborated by the absence of saturation of the pump light absorption by the sample within the range of pump pulse energy of the experiment ($<4 \mu\text{J}$). Deviation from the linearity of the pump-induced absorption was observed only at much higher pump pulse energies of $>20 \mu\text{J}$.

Using a simple two-state model, effective microscopic hyperpolarizability (β_{eff}) of the photoexcited nanocrystal can be represented as a linear sum of contributions from valance and conduction band electrons.

$$\beta_{\text{eff}} = N_v \beta_v + N_c \beta_c$$

N_v and N_c are the valance and conduction band electron densities, respectively. β_v and β_c are the valance and conduction band contributions to the hyperpolarizability, which are constants. In this case, $\chi_{\text{rel,peak}}^{(2)}$ will exhibit a linear increase with respect to the pump pulse energy in the linear excitation regime. A similar two-level model has been previously employed to explain the pump-induced changes of SHG signal in a number of systems including surfaces and a single nanocrystal.^{20,22,24} Figure 3 shows the plot of the $\chi_{\text{rel,peak}}^{(2)}$ vs pump pulse energy for two different sizes of spherical CdTe nanocrystals (7 and 13 nm). Approximate electron–hole densities at corresponding pulse energies are also indicated on the top axis. In this figure, $\chi_{\text{rel,peak}}^{(2)}$ increases linearly at lower pump pulse energies (e.g., below $1 \mu\text{J}$), but becomes sublinear at higher pump pulse energies. The data are fit to $\chi_{\text{rel,peak}}^{(2)} = c \cdot [1 - \exp(-x/x_0)] + 1$, analogous to the exponential saturation curve, to clearly show the sublinearity. The pump pulse energy dependence of $\chi_{\text{rel,peak}}^{(2)}$ is not sensitive to the size of the nanocrystals used in this study. However, the measured absolute SHG signals were stronger for the samples of larger nanocrystals for a given number of total CdTe units in the sample solution. This is consistent with the findings of Jacobsohn et al., where the β value per nanocrystal increases with the size of the nanocrystal.¹⁷

The sublinear increase of $\chi_{\text{rel,peak}}^{(2)}$ means that the average one-electron second-order nonlinearity of electrons excited to the conduction band diminishes as the carrier density increases in the nanocrystals. Although a number of factors have been suggested to explain electron–hole density-dependent second-order nonlinearity, such as bond charge, local field effect,

symmetry of lattice, and charge distribution etc., current understanding on this issue still remains crude.⁹ The simplest explanation for the sublinear increase of $\chi_{\text{rel,peak}}^{(2)}$ may be the formation of the electron–hole plasma at higher electron–hole densities. As the electron–hole density increases, initially bound electron–hole pairs form an electron–hole plasma due to the diminishing electron–hole interaction. The dense and noninteracting electron–hole plasma may effectively experience a less anharmonic force field from the lattice than the bound electron–hole pairs, responding more harmonically to the external electric field. This can explain the decreasing one-electron second-order susceptibility with increasing electron–hole density. An alternative explanation is the involvement of the plasmon resonance in the SHG process. As the electron–hole density varies with the pump pulse energy, the plasmon resonance frequency sweeps from lower to higher frequencies. This can result in pump-energy-dependent resonance enhancement of the SHG with the peak enhancement occurring at a particular electron–hole density. The monotonic sublinear increase of $\chi_{\text{rel,peak}}^{(2)}$ observed in this study, however, can be more readily explained using the former argument.

While the argument involving the electron–hole plasma is a plausible explanation for the observed sublinear increase of $\chi_{\text{rel,peak}}^{(2)}$, it cannot be directly associated with a bulklike exciton/electron–hole plasma transition. In nanocrystals that impose a spatial confinement (e.g., 7 nm CdTe), the bulk exciton Mott transition loses its meaning because a single electron–hole pair already exceeds the Mott transition density while it is still bound. So far, a direct experimental observation of such transition in semiconductor nanocrystals with three-dimensional spatial confinement has not been made.²⁵ In Figure 3, the estimated electron–hole density at the best fitting parameter x_0 for the exponential saturation curve is $\sim 8 \cdot 10^{20}/\text{cm}^3$. On the basis of the foregoing discussion, this may be qualitatively interpreted as the electron–hole density, where the charge carriers change their character from bound pairs to free plasma.²⁶ In this study, CdTe nanocrystals of two different sizes (7 and 13 nm) were used to represent the relatively strong and the weak confinement regime, respectively (bulk exciton Bohr radius = 7.5 nm). The two samples exhibit only a small difference in $\chi_{\text{rel,peak}}^{(2)}$ at higher pump energies, without significant size dependence. However, because of the limited set of size-dependent data of this study, we cannot make a conclusive remark on the size dependence of $\chi_{\text{rel,peak}}^{(2)}$ at this point. Further studies with nanocrystals of broader size range will be necessary in order to reach a more definitive conclusion.

As mentioned previously, because of the increased noise, we could not access the higher pump intensity regime of the transient SHG response, and we were far from accessing the pump intensity required for melting. For that higher intensity regime, while still overlapping with the present regime, we followed a different physical probe, that of the power dependence of the coherent acoustic phonons.

3.2. Coherent Confined Acoustic Phonon in CdSe Nanocrystals. Coherent phonons can be excited by the optical excitation of electron–hole pairs in semiconductor materials through various electron–phonon coupling mechanisms. Depending on the specific mechanism, coherent phonons can be excited in optical and/or acoustic modes. In nanocrystals, the frequency of the acoustic mode exhibits size dependence, whereas the optical mode is only weakly dependent on the size of the nanocrystals.²⁷ The effect of the surface and the size of the nanocrystals on the excitation of coherent acoustic phonons has been a subject of interest in earlier studies.¹⁴ Here, as in

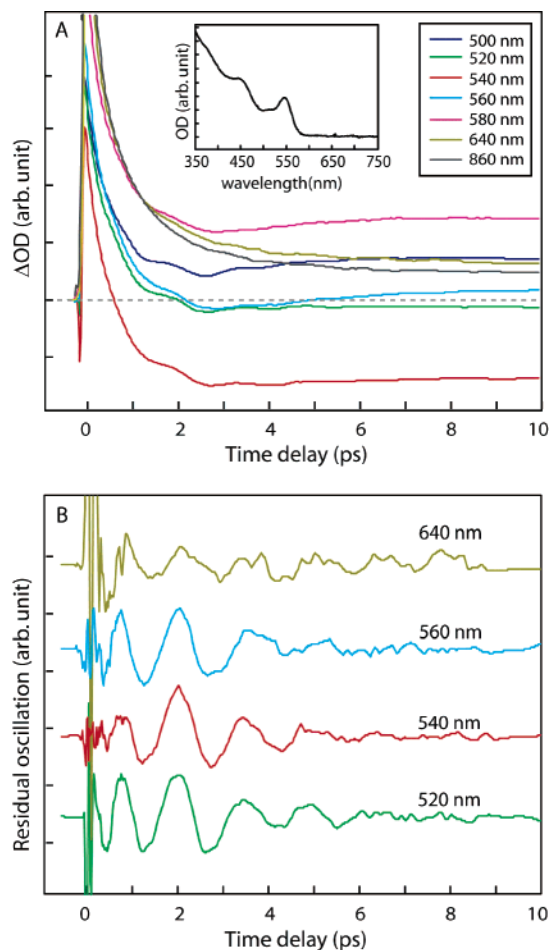


Figure 4. (A) Pump-probe time-resolved absorption data from CdSe nanocrystals obtained with an intense 400 nm pump ($\sim 30 \mu\text{J}$ pulse energy) and the continuum probe. The inset is the static absorption spectrum of the CdSe nanocrystal sample solution. A dotted horizontal line indicates zero ΔOD . (B) The isolated oscillatory feature from the time-resolved absorption data at selected probe wavelengths across the first excitonic absorption peak at 550 nm.

the previous section on SHG, we investigated the pump pulse energy dependence as part of our interest in probing the nanocrystals in the strong excitation regime, leading eventually to melting. We also compared the response of the acoustic phonons between spherical and rod shaped particles.

Excitation of coherent phonons in nanocrystals is relatively easily seen in the time-resolved absorption data. Figure 4A shows the time-resolved absorption data of CdSe nanocrystals obtained with 400 nm pump and continuum probe light. The static absorption spectrum of the sample is shown in the inset. While oscillatory features superimposed on the slowly varying absorption traces were discernible, they become less distinct at low excitation intensity probe wavelengths much longer than the band gap of the nanocrystal (e.g., as in Figure 2B). These oscillations are due to the modulation of the band gap and absorption cross section by the coherent acoustic phonons of the nanocrystals. The main mechanisms for the excitation of coherent acoustic phonons in semiconductors are acoustic deformation potential coupling, piezoelectric coupling, and impulsive heating of the lattice by rapid relaxation of charge carriers.^{27,28} In CdSe nanocrystals under weak excitation, deformation potential coupling is considered to be the dominant mechanism.¹⁴ In Figure 4B, the oscillatory parts of the time-resolved absorption data are shown for several probe wavelengths near the first excitonic absorption peak (550 nm). There

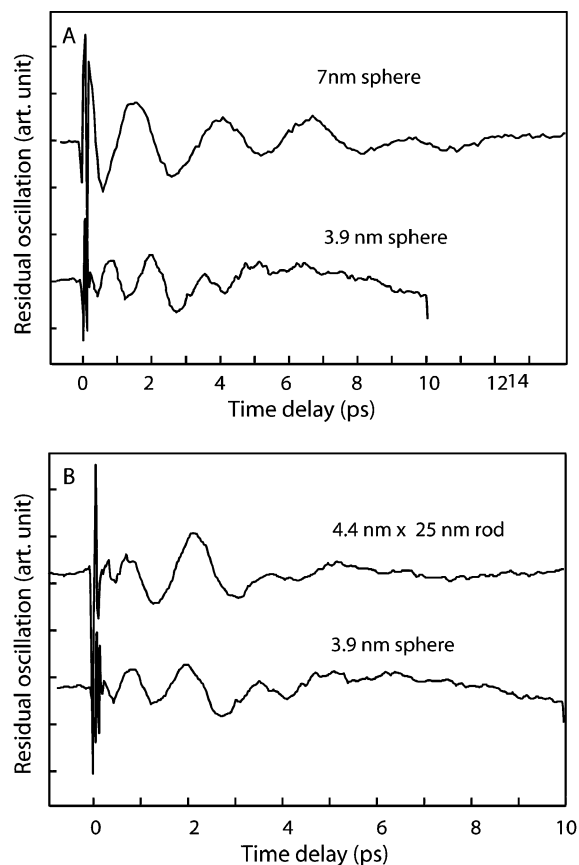


Figure 5. (A) Comparison of the oscillations in time-resolved absorption data of the two spherical CdSe nanocrystals of different size. (B) Comparison of the oscillations in time-resolved absorption data of the spherical and the rod-shape CdSe nanocrystals.

is no observable phase shift of the oscillation across the first excitonic absorption peak, and the phases are almost constant at all probe wavelengths. The absence of a phase shift is probably because the bleach of the first excitonic absorption does not recover during the period of time the oscillations are observed under the relatively strong excitation conditions of this study. The slow recovery of the excitonic absorption results in a more featureless absorption line shape. Therefore, band gap modulation is primarily responsible for the observed oscillation. This is in contrast to what was observed in gold nanocrystals, where the shift of the plasmon resonance peak results in a 180° phase shift of the oscillation when the probe wavelength is varied across the peak of the plasmon absorption.²⁹

In Figure 5A, a comparison of the oscillatory parts is made between the two CdSe nanocrystal samples of 3.9 and 7 nm in diameter, obtained with a 400 nm pump and a 520 nm probe. The oscillation frequencies determined by Fourier transformation are 24 and 13 cm^{-1} for 3.9 and 7 nm nanocrystals, respectively.³⁰

The size dependence of the frequency and dephasing time of the coherent acoustic modes in spherical nanocrystals has been previously investigated by Cerullo et al. for InAs nanocrystals.¹⁴ The frequencies of the acoustic modes were inversely proportional to the diameters of the nanocrystals and are well explained by a continuum model describing the confined radial breathing mode using bulk elastic constants. Slower dephasing in larger nanocrystals was ascribed to the smaller surface area per volume, which acts as the window for coherence loss. Our observations made for spherical CdSe nanocrystals are in accordance with the findings of Cerullo et al. We observed a lower acoustic mode frequency for the larger dots as mentioned above and also that

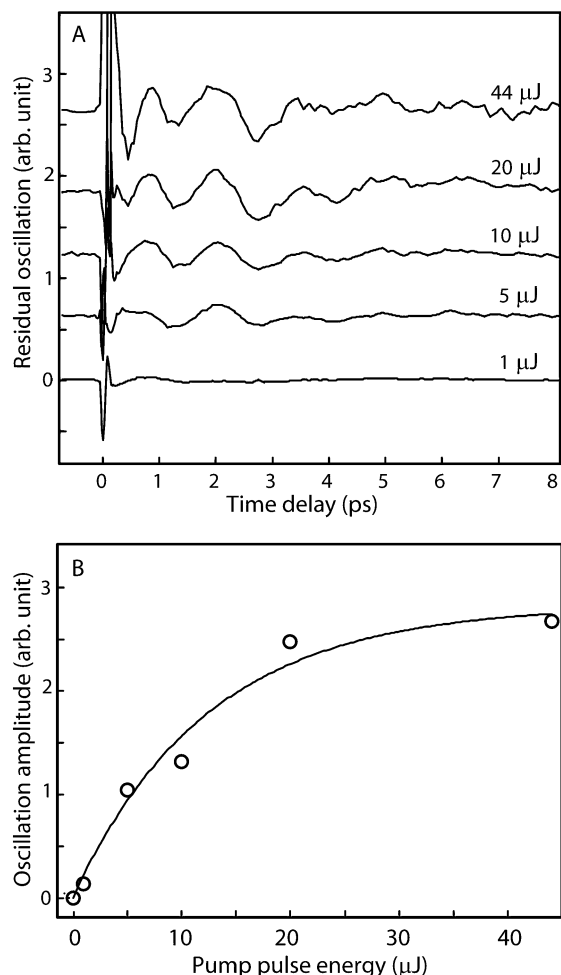


Figure 6. (A) Pump pulse energy dependence of the oscillation in CdSe nanocrystals. (B) Pump pulse energy dependence of the oscillation amplitude in spherical CdSe nanocrystals.

the dephasing of the oscillations is slower in the larger nanocrystals.

Sensitivity of the response of the coherent acoustic phonons to the nanocrystal shape was studied next. Figure 5B compares the oscillations of a nanosphere and nanorod, whose radii are similar. While there is one isotropic radial mode in a spherical nanocrystal, there are transverse and longitudinal modes in a nanorod. Although the two modes in the nanorod are not strictly separable, transverse and longitudinal mode frequencies are dependent on the width and length of the nanorod, respectively.³¹ In Figure 5B, both the sphere and the rod exhibit similar oscillation periods. This indicates that the observed oscillations in the nanorod reflect mostly the transverse (radial) mode of the coherent phonons. This is consistent with the fact that the band gap in a nanorod is primarily determined by the width rather than the length of the rod.³² Although only the changes in the linear absorption have been observed in this study, other higher-order optical properties can be affected by coherent phonons in principle. In the bulk, modulation of the surface second harmonic signal has been observed after exciting coherent surface phonons.¹⁵ In this study, we have not observed the effect of coherent acoustic phonons on second harmonic signals from the spherical CdTe nanocrystals discussed in the previous section, possibly due to the radial symmetry of the breathing mode.

In Figure 6A, the pump-energy-dependent oscillations in spherical CdSe nanocrystals are shown for a broad range of excitation energies. The frequency and phase of the oscillation

do not show noticeable dependence on the pump pulse energy. This indicates that the elastic constants of the nanocrystals do not depend significantly on the level of excitation. It should be mentioned, however, that the restoring force between the atoms can be weakened significantly under strong excitation before carrier relaxation occurs. Such softening of the lattice is responsible for nonthermal melting in many semiconductors and can persist long enough to be seen via the frequency shifting of optical phonons.³³ The influence of lattice softening on acoustic phonons, on the other hand, may not be clearly observable due to the relatively long oscillation period (> 1 ps) compared to the time scale of lattice softening by dense electron–hole pairs.

The amplitudes of the oscillations in Figure 6A exhibit an increase as the pump pulse energy increases. While the frequency of the confined acoustic mode has a relatively well-established relationship to material parameters, such as the elastic constants, the amplitude of the oscillation is a more complex problem.³⁴ In a simple picture of acoustic deformation potential coupling, the band gap shift is proportional to the compression or expansion of the lattice.³⁵ In this case, a simple linear relationship between the oscillation amplitude and the atomic displacement may be obtained if the slope of the absorption vs wavelength does not change much. In reality, this is an oversimplification, especially at early delay times before the relaxation of the carriers, because both the electronic structure and the restoring force between the atoms are altered under strong excitation. Nevertheless, oscillation amplitudes measured at delay times later than the carrier relaxation time may still provide useful information on the relative amplitudes of lattice displacement at various pump pulse energies. Figure 6B shows the pump pulse energy dependence of the relative oscillation amplitudes. The amplitudes are measured simply by taking the peak-to-peak amplitude for one oscillation cycle at the time delays of 2–3 ps, ignoring possible dependence of dephasing time on the pump intensity. The increase of the oscillation amplitude with pump pulse energy can be interpreted as an increase of the amplitude of the coherent lattice displacement. Within the simple picture discussed above, the saturation of the oscillation amplitude in Figure 6B suggests the saturation of the lattice displacement. It should be pointed out, however, that the purely optical measurement has limited capability of probing the structural changes of the crystalline materials. More quantitative information on lattice displacements should be obtained by using another experimental method to directly probe the crystal structures, such as time-resolved diffraction or X-ray absorption.

4. Discussion

The two different phenomena we studied, SHG and coherent acoustic phonons, are sensitive to different aspects of the highly excited nanocrystal dynamics. SHG in nanocrystals is due to the nonlinearity in the electronic response, while coherent acoustic phonons are sensitive to the elastic properties of the nanocrystals. We found that both phenomena depend on the excitation intensity. The SHG shows an initial enhancement in the transient response, attributed to the increased nonlinearity of the highly excited electrons, and indeed exhibited a rapid decay, consistent with the rapid decay time of the excited carriers in nanocrystals. Our hope to approach the melting regime with this method did not materialize due to increased noise at the higher excitation powers. We expected to see the signal inverting to a reduction in SHG signal upon the occurrence of melting, leading to disorder of the crystal lattice as observed in bulk

semiconductors.³⁶ Although we could not access this regime, we observed early saturation of the enhancement in the SHG signal with pump intensity. It may still be possible to observe a decrease in SHG upon higher excitation powers, using a different probe wavelength not presently accessible to us, which would reduce the noise.

Unlike the SHG, which is strongly sensitive to the electronic contribution and carrier dynamics, the coherent acoustic phonons depend mostly on the size of the particles. Here we also observed enhancement of the amplitude of the signal under increased excitation intensity. We could access a much broader intensity regime, up to levels close to where we expect the onset of melting. The saturation of the transient acoustic phonon amplitude is observed at significantly higher powers compared to that of the SHG enhancement. On the other hand, the frequency of the acoustic phonon was sensitive to the nanocrystal size, particularly the radius in the case of rods, but not to the excitation intensity. The insensitivity of acoustic phonon to the excitation intensity makes it a rather poor probe for detecting melting in spherical nanocrystals of several nanometers. This is because the sufficiently large changes in size and the elastic properties upon melting are not expected to persist long enough to be detected in the acoustic phonon. The mode coupling, which depends on the deformation potential, is also not expected to show a dramatic change upon melting. As mentioned above, a proper probe such as time-resolved X-ray diffraction or absorption will be needed to directly provide structural information.

5. Conclusions

We have investigated the photoinduced enhancement of incoherent second harmonic generation and the shape and pump intensity dependence of the coherent acoustic phonons in semiconductor nanocrystals under intense photoexcitation. As the photoexcited electron–hole density increased, the SHG signal from the nanocrystals also increased, indicating that the second-order electric susceptibility is higher for the conduction band electrons than the valence band electrons. The increase of the second-order susceptibility is sublinear to the pump pulse energy, indicating that the effective one-electron second-order nonlinearity diminishes with increasing electron–hole density. The coherent acoustic phonons in spherical and rod-shaped semiconductor nanocrystals were detected in the time-resolved absorption measurement. Both nanocrystals exhibited an oscillatory modulation of the absorption cross section, whose frequencies correspond to the coherent radial breathing modes. The amplitude of the oscillation also increased with the level of photoexcitation, suggesting an increase in the amplitude of the lattice displacement as well.

Acknowledgment. This work was supported by U.S. Department of Energy under the contract number DE-AC02-05CH11231, Department of Defense, Air Force Office of Scientific Research under the contract number FA 9550-04-1-0242. Partial support of the U.S.–Israel Binational Science Fund (BSF) is acknowledged. We thank Prof. Dung-hai Lee of Department of Physics at University of California, Berkeley for helpful discussions.

References and Notes

- (1) Murray, C. B.; Norris, D. J.; Bawendi, M. C. *J. Am. Chem. Soc.* **1993**, *115*, 8706.
- (2) Peng, X.; Manna, L.; Yang, W.; Wickham, J.; Scher, E. C.; Kadavanich, A.; Alivisatos, A. P. *Nature* **2000**, *404*, 59.
- (3) Franceschetti, A.; Zunger, A. *Phys. Rev. Lett.* **1997**, *78*, 915.
- (4) Klimov, V. I.; Mikhailovsky, A. A.; McBranch, D. W.; Leatherdale, C. A.; Bawendi, M. G. *Science* **2000**, *287*, 1011.
- (5) Burda, C.; Link, S.; Mohamed, M. B.; El-Sayed, M. J. *Chem. Phys.* **2002**, *116*, 3828.
- (6) Son, D. H.; Wittenberg, J. W.; Alivisatos, A. P. *Phys. Rev. Lett.* **2004**, *92*, 127406.
- (7) Shank, C. V.; Fork, R. L.; Leheny, R. F.; Shah, J. *Phys. Rev. Lett.* **1972**, *42*, 112.
- (8) Nagaia, M.; Kuwata-Gonokami, M. *J. Lumin.* **2002**, *100*, 233.
- (9) Linde, D. v. d. *Annu. Rev. Mater. Sci.* **1988**, *18*, 75.
- (10) Shank, C. V.; Yen, R.; Hirsimann, C. *Phys. Rev. Lett.* **1983**, *50*, 454.
- (11) Sokolowski-Tinten, K.; Bialkowski, J.; Boing, M.; Cavalleri, A.; Linde, D. v. d. *Phys. Rev. B* **1998**, *58*, R11805–R11808.
- (12) Goldstein, A. N.; Echer, C. M.; Alivisatos, A. P. *Science* **1992**, *256*, 1425.
- (13) In transmission electron micrographs, morphology change of rod-shaped semiconductor nanocrystals resulting from melting was observed under a more intense excitation condition. Unpublished result.
- (14) Cerullo, G.; De Silvestri, S.; Banin, U. *Phys. Rev. B* **1999**, *60*, 1928.
- (15) Chang, Y. M.; Xu, L.; Tom, H. W. K. *Phys. Rev. Lett.* **1997**, *78*, 4649.
- (16) Bennemann, K. H. *J. Phys.: Condens. Matter* **2004**, *16*.
- (17) Jacobssohn, M.; Banin, U. *J. Phys. Chem. B* **2000**, *104*, 1.
- (18) Hendrickx, E.; Clays, K.; Persoons, A. *Acc. Chem. Res.* **1998**, *31*, 675.
- (19) Papadogiannis, N. A.; Moustazis, S. D. *Opt. Commun.* **1997**, *137*, 174.
- (20) Bodlaki, D.; Borguet, E. *Appl. Phys. Lett.* **2003**, *83*, 2357.
- (21) Petrov, D. V.; Faustino, W. M. *Opt. Commun.* **2002**, *203*, 145.
- (22) Johnson, J. C.; Knutsen, K. P.; Yan, H.; Law, M.; Zhang, Y.; Yang, P.; Saykally, R. J. *Nano Lett.* **2004**, *4*, 197.
- (23) Guo, C.; Rodriguez, G.; Taylor, A. J. *Phys. Rev. Lett.* **2001**, *86*, 1638.
- (24) McClelland, A.; Fomenko, V.; Borguet, E. *J. Phys. Chem. B* **2004**, *108*, 3789.
- (25) Kappei, L.; Szczytko, J.; Morier-Genoud, F.; Deveaud, B. *Phys. Rev. Lett.* **2005**, *94*, 147403.
- (26) The carrier density is calculated from the average fluence under the probe area (4.5 mJ/cm²) and the approximate absorption cross section of 7 nm CdTe nanocrystal at 400 nm (1.5×10^{-14} cm²). The absorption cross section of CdTe nanocrystals was calculated from the UV–vis absorption spectrum and the concentration of the nanocrystals. The concentration of CdTe nanocrystal solution was determined from the measurement of atomic absorption of Cd²⁺ ions in the sample referenced to the standard Cd²⁺ solution.
- (27) Krauss, T. D.; Wise, F. W. *Phys. Rev. Lett.* **1997**, *79*, 5102.
- (28) Lindenberg, A. M.; Kang, I.; Johnson, S. L.; Missalla, T.; Heimann, P. A.; Chang, Z.; Larsson, J.; Bucksbaum, P. H.; Kapteyn, H. C.; Padmore, H. A.; Lee, R. W.; Wark, J. S.; Falcone, R. W. *Phys. Rev. Lett.* **2000**, *84*, 111.
- (29) Hartland, G. V. *J. Chem. Phys.* **2002**, *116*, 8048.
- (30) At time delays <0.5 ps, oscillation amplitudes are less accurate because the fitting and subtraction procedure has larger error than those in later delay times. In the Fourier transformation of the oscillations for the analysis of the frequency, only the traces after 0.5 ps are used.
- (31) Hu, M.; Wang, X.; Hartland, G. V.; Mulvaney, P.; Juste, J. P.; Sader, J. E. *J. Am. Chem. Soc.* **2003**, *125*, 14925.
- (32) Li, L. S.; Hu, J. T.; Yang, W. D.; Alivisatos, A. P. *Nano Lett.* **2001**, *1*, 349.
- (33) Hunsche, S.; Wienecke, K.; Dekorsy, T.; Kurz, J. *Phys. Rev. Lett.* **1995**, *75*, 1815.
- (34) Strosio, M. A.; Kim, K. W.; Yu, S.; Ballato, A. *J. Appl. Phys.* **1994**, *76*, 4670.
- (35) Takagahara, T. *J. Lumin.* **1996**, *70*, 129.
- (36) Saeta, P.; Wang, J. K.; Siegal, Y.; Bloembergen, N.; Mazur, E. *Phys. Rev. Lett.* **1991**, *67*, 1023.